



CHORUS

This is the accepted manuscript made available via CHORUS. The article has been published as:

Kekulé-induced valley birefringence and skew scattering in graphene

Elias Andrade, Ramon Carrillo-Bastos, Mahmoud M. Asmar, and Gerardo G. Naumis

Phys. Rev. B **106**, 195413 — Published 14 November 2022

DOI: [10.1103/PhysRevB.106.195413](https://doi.org/10.1103/PhysRevB.106.195413)

Kekulé Induced Valley Birefringence and Skew Scattering in Graphene

Elias Andrade,^{1,*} Ramon Carrillo-Bastos,² Mahmoud M. Asmar,³ and Gerardo G. Naumis⁴

¹*Posgrado en Ciencias Físicas, Instituto de Física, Universidad Nacional Autónoma de México (UNAM). Apdo. Postal 20-364, 01000 México D.F., México*

²*Facultad de Ciencias, Universidad Autónoma de Baja California, Apdo. Postal 1880, 22800 Ensenada, Baja California, México.*

³*Department of Physics, Kennesaw State University, Marietta, Georgia 30060, U.S.A.*

⁴*Depto. de Sistemas Complejos, Instituto de Física, Universidad Nacional Autónoma de México (UNAM). Apdo. Postal 20-364, 01000 México D.F., México*

(Dated: November 2, 2022)

In graphene, a Kekulé-Y bond texture modifies the electronic band structure generating two concentric Dirac cones with different Fermi velocities lying in the Γ -point in reciprocal space. The energy dispersion results in different group velocities for each isospin component at a given energy. This energy spectrum combined with the negative refraction index in p-n junctions, allows the emergence of an electronic analog of optical birefringence in graphene. We characterize the valley birefringence produced by a circularly symmetric Kekulé patterned and gated region using the scattering approach. We found caustics with two cusps separated in space by a distance dependent on the Kekulé interaction and that provides a measure of its strength. Then, at low carrier concentration we find a non-vanishing skew cross section, showing the asymmetry in the scattering of electrons around the axis of the incoming flux. This effect is associated with the appearance of the valley Hall effect as electrons with opposite valley polarization are deflected towards opposite directions.

I. INTRODUCTION

The similarities between the Helmholtz and Schrödinger equations result in photons and electrons displaying similar wave phenomena¹. Furthermore, the propagation of electrons through the two-dimensional honeycomb arrangement of carbon atoms, known as graphene, leads to the dressing of electronic states as massless Dirac-like electronic excitations residing at opposite corners of the Brillouin zone², thus augmenting the analogies between the electronic and optical phenomena. The ability to control the charge carriers group velocity via graphene gating³ has led to the prediction and experimental realization of electronic Veselago lensing, where incoming divergent rays become convergent after refraction on a flat surface with a negative index of refraction^{4,5}. The sensitivity of this lensing to the conduction electrons properties aids the detection of anisotropies and tilting of the Dirac cones^{6,7}, the presence of strain⁸, and disorder⁹. Veselago lensing also facilitates the waveguiding of electrons in p-n junctions^{10,11} and in circular geometries¹² as well as the emergence of caustics (wave envelopes of refracted electrons) which often have cusp singularities. Moreover, similar to optical birefringence in anisotropic crystals, where the group velocity depends on light polarization¹³ and thus incoming light rays can be split in two, spin birefringence for electrons emerges in graphene due to the Rashba spin-orbit interaction^{14,15} which leads to distinct Fermi velocities for each spin component. In circular geometries, spin birefringence brings about the formation of caustics with two cusps, with a space separation that depends on the strength of the Rashba spin-orbit coupling^{16,17}. However, spin-orbit interactions in graphene are small which the detection

of spin-birefringence experimentally challenging.

In addition to spin, electrons in graphene possess the valley degree of freedom¹⁸. The valleys in graphene have a large separation in momentum space¹⁹, which suggests that this degree of freedom can be potentially used in applications where it will play a role similar to spin in spintronics^{20,21}. The field that aims to manipulate and control the valley degree of freedom in applications is known as *valleytronics*²²⁻³⁴. Similar to spin-orbit interactions in spintronics, interactions contrasting the degenerate valleys in graphene play an essential role in valleytronics. Such interactions include the Kekulé patterning of graphene^{35,36}, *i.e.*, the periodic bond modulation of the graphene lattice. Depending on the bond modulation pattern³⁷ two different Kekulé distortions phases can emerge: the Kekulé-Y³⁸ found in graphene deposited on Cu[111] and the Kekulé-O³⁹⁻⁴³ that arises in bilayer graphene intercalated with Li. The tight-binding calculations by Gamayun *et al.*³⁷ found that Kekulé-Y produces an effective interaction that leads to valley-momentum locking, while Kekulé-O leads to the formation of a gap in the electronic spectrum.

Kekulé-Y patterned graphene, breaks a valley degeneracy through valley-momentum locking which produces a low energy spectrum with two nested Dirac cones with different Fermi velocities³⁷. The energy-momentum dispersion modification caused by Kekulé-Y patterning leads to drastic modifications in the magnetic and optical response of graphene⁴⁴⁻⁴⁹, and crucially aids the control of the valley degree of freedom in the electronic transport⁵⁰⁻⁵⁷. In this paper we study the scattering of Dirac fermions from circularly Kekulé-Y-patterned regions in the semiclassical limit and we explore the effects of this interaction on electron optics and the appearance of valley birefringence. We also investigate the scattering

of charge carriers in graphene from short-range scattering regions with locally enhance Kekulé-Y interactions due to adatom deposition. Our analysis of the total, transport, and skew cross sections for these short-range scatterers reveals the dependence of these cross sections on the strength of the Kekulé-Y interaction and we show the appearance of a valley Hall effects due to skew scattering from these scatterers.

The layout of this work is as follows. In section II we present the model, section III is devoted the scattering calculations. Valley birefringence is analyzed in section IV, while in section V we study the low-energy scattering. Finally, we conclude by discussing our main findings.

II. MODEL

Our system consist of an infinite sheet of pristine graphene containing a circularly Kekulé-ordered patch of radius R , Fig. 1. We consider the scattering of an incoming flux of electrons in the x -direction with momentum k . To describe the electronic properties of the graphene sheet we adopt the low-energy description, i.e., the Dirac Hamiltonian¹⁹. Nevertheless, the Kekulé modulated portion of the lattice has a larger unit cell than non-modulated graphene lattice. Hence, to match the pristine and Kekulé patterned graphene wave functions it is practical to use an enlarged unitary cell for the case of undistorted graphene. This is equivalent to consider the group C_{6v}'' , with a cell with six atom graphenes unit cell, which avoids the treatment of degenerate states at two inequivalent Dirac points⁵⁸. This is more clearly seen if we start with the Hamiltonian for the Kekulé region and then pristine graphene appears as a limiting case.

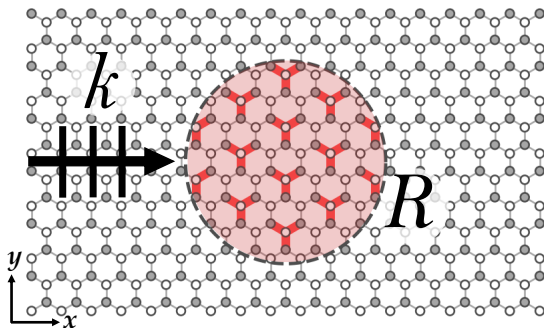


FIG. 1. Schematic of the system (not to scale). A graphene lattice where an incoming flux of electrons in the x direction approaches a circular region of radius R with a gate potential and Kekulé-Y bond texture (red bonds).

The space dependent Hamiltonian describing the system in Fig. 1 is given by

$$\mathcal{H} = \mathcal{H}_0 + \mathcal{H}_Y(r) + V(r), \quad (1a)$$

where,

$$\mathcal{H}_0 = v_f(\mathbf{p} \cdot \boldsymbol{\sigma}) \otimes \tau_0 \quad (1b)$$

is the low-energy graphene Hamiltonian with $\mathbf{p} = -i\hbar(\partial_x, \partial_y)$ the momentum operator, $v_f \sim 10^6$ m/s the Fermi velocity, and σ, τ the sets of Pauli matrices acting on the sublattice and valley pseudo-spin spaces respectively.

$$\mathcal{H}_Y = \Delta v_f \sigma_0 \otimes (\mathbf{p} \cdot \boldsymbol{\tau}) \Theta(R - r) \quad (1c)$$

is the Kekulé-Y bond perturbation³⁷ with amplitude Δ within the circular region,

$$V(r) = V_0 \Theta(R - r) \sigma_0 \otimes \tau_0, \quad (1d)$$

is a constant gate potential with amplitude V_0 in the Kekulé circular patch, and Θ is the Heaviside function.

The Hamiltonian in Eq. (1a) acts on the states expressed in the valley isotropic representation⁵⁹:

$$\Psi = \begin{bmatrix} \psi_{K'} \\ \psi_K \end{bmatrix} = \begin{bmatrix} -\psi_{B,K'} \\ \psi_{A,K'} \\ \psi_{A,K} \\ \psi_{B,K} \end{bmatrix}, \quad (1e)$$

notice that the subindex A and B in Ψ corresponds to each graphene's bipartite lattice while \mathbf{K} and \mathbf{K}' label the valley. For regions outside the Kekulé modulated region, the limit of pristine graphene is recovered, $\Delta = 0$, thus having a 4×4 operator which represents the Dirac Hamiltonian in the enlarged unitary cell.

III. SCATTERING

In this section we study the scattering of Dirac fermions from a circularly symmetric Kekulé patterned region. We adopt the partial waves scattering method to find the S-matrix, which requires finding and matching the eigenstates in the different scattering regions of our system. For any effective theory that uses an envelope wavefunction, as is the case of the Dirac equation for graphene, the matching requires a supplemental boundary condition of the form $\Psi = M\Psi$ in order to retain the hermiticity and preserve currents. Here M is a matrix containing the microscopic details and the symmetries of the problem⁵⁹⁻⁶⁴. Since we consider the Kekulé-Y bond modulation as a perturbation within the same graphene sheet, no major misalignment is expected and thus for small Δ we can consider M as unitary throughout this work. Here we note that we are using a low-energy approximation near the Fermi level for Kekulé-Y graphene. As in pristine graphene, the effective equation is circular symmetric³⁷. At energies away from the Fermi level the discrete nature of the lattice is initially reflected via trigonal warping. This part of the spectrum is not sampled by fermions near the Fermi energy as is only visible on other scales of energy. Therefore, we can

safely treat our system as circular symmetric and thus is natural to evaluate its eigenfunctions in polar coordinates. The z -component of orbital angular momentum $L_z = -i\hbar\partial_\theta$ does not commute with the Hamiltonian, $[H, L_z] = i\hbar v_f(\boldsymbol{\sigma} \times \mathbf{p})_z \otimes \tau_0 + i\hbar v_f \sigma_0 \otimes (\boldsymbol{\tau} \times \mathbf{p})_z$. On the other hand, the sum of L_z and the intrinsic angular momenta associated with the valley and sublattice degrees of freedom, “valley-lattice-angular momentum” J_z , is conserved and given by

$$J_z = L_z + \frac{\hbar}{2}(\sigma_z \otimes \tau_0 + \sigma_0 \otimes \tau_z). \quad (2)$$

Here, it is important to notice that $[H, \frac{\hbar}{2}\sigma_z \otimes \tau_0] = -i\hbar v_f(\boldsymbol{\sigma} \times \mathbf{p})_z \otimes \tau_0$, and $[H, \frac{\hbar}{2}\sigma_0 \otimes \tau_z] = -i\hbar v_f \sigma_0 \otimes (\boldsymbol{\tau} \times \mathbf{p})_z$, which leads to $[H, \frac{\hbar}{2}\sigma_z \otimes \tau_0 + \frac{\hbar}{2}\sigma_0 \otimes \tau_z + L_z] = 0$. We can express the eigenfunctions in their total pseudo-angular momentum basis, such that $J_z \Psi_m = m\hbar \Psi_m$, thus

$$\Psi_m(r, \theta) = e^{im\theta} \begin{bmatrix} -e^{-i\theta} \Phi_{B, K'}(r) \\ \Phi_{A, K'}(r) \\ \Phi_{A, K}(r) \\ e^{i\theta} \Phi_{B, K}(r) \end{bmatrix}, \quad (3)$$

where $\theta = \tan^{-1} y/x$, and find the radial part of the wave functions by applying the Hamiltonian in Eq. (1a) to our spinor in Eq. (3) to get the following set of coupled differential equations,

$$L_m^- [\Phi_{A, K'}(r) + \Delta \Phi_{A, K}(r)] = -i(\epsilon - \nu) \Phi_{B, K'}(r), \quad (4a)$$

$$L_{m-1}^+ \Phi_{B, K'}(r) - \Delta L_{m+1}^- \Phi_{B, K}(r) = -i(\epsilon - \nu) \Phi_{A, K'}(r), \quad (4b)$$

$$L_{m+1}^- \Phi_{B, K}(r) - \Delta L_{m-1}^+ \Phi_{B, K'}(r) = i(\epsilon - \nu) \Phi_{A, K}(r), \quad (4c)$$

$$L_m^+ [\Phi_{A, K}(r) + \Delta \Phi_{A, K'}(r)] = i(\epsilon - \nu) \Phi_{B, K}(r), \quad (4d)$$

where,

$$L_m^\pm = \left(\partial_r \mp \frac{m}{r} \right), \quad (4e)$$

here $\epsilon = E/(\hbar v_f)$, $\nu = V_0/(\hbar v_f)$. Since L_m^\pm acts as a ladder operator for the cylindrical Bessel functions J_m ,

$$L_m^\pm J_m(kr) = \mp k J_{m\pm 1}(kr), \quad (5)$$

thus, a natural ansatz is

$$\Phi_{A, K}(r) = i(\epsilon - \nu) C_A J_m(kr), \quad (6)$$

$$\Phi_{A, K'}(r) = i(\epsilon - \nu) C_B J_m(kr), \quad (7)$$

where C_A and C_B are constants, and k is the electron wave number. Inserting the ansatz in Eq. (6) in the relations in Eq. (4), results into the exact form of the spinor solutions and determines the wave numbers

$$k_\pm = \frac{|E - V_0|}{\hbar v_f (1 \pm \Delta)}. \quad (8)$$

Thus the m^{th} angular momentum eigenstates in the inner region are,

$$\Psi_m^{(\text{inner})}(r, \theta) = T_m^+ e^{im\theta} \begin{bmatrix} J_{m-1}(k_+ r) e^{-i\theta} \\ i s' J_m(k_+ r) \\ i s' J_m(k_+ r) \\ -J_{m+1}(k_+ r) e^{i\theta} \end{bmatrix} + T_m^- e^{im\theta} \begin{bmatrix} J_{m-1}(k_- r) e^{-i\theta} \\ i s' J_m(k_- r) \\ -i s' J_m(k_- r) \\ J_{m+1}(k_- r) e^{i\theta} \end{bmatrix}, \quad (9)$$

where T_m^+ and T_m^- are determined by $s' = \text{sgn}(E - V_0)$ and the boundary conditions. Since the pseudo-angular momentum is conserved during the scattering process, we can treat each component of m independently and use the partial wave method to determine the S-matrix elements. In the region $r > R$, we describe the wavefunction in terms of incoming (in) and outgoing (out) cylindrical waves, where the corresponding spinor for each valley is

$$\psi_{m, K'}^{(\text{out})/(\text{in})}(r, \theta) |K'\rangle = \begin{bmatrix} H_{m-1}^{(1)/(2)}(kr) e^{i(m-1)\theta} \\ i s H_m^{(1)/(2)}(kr) e^{im\theta} \end{bmatrix} |K'\rangle, \quad (10a)$$

$$\psi_{m, K}^{(\text{out})/(\text{in})}(r, \theta) |K\rangle = \begin{bmatrix} -i s H_m^{(1)/(2)}(kr) e^{im\theta} \\ H_{m+1}^{(1)/(2)}(kr) e^{i(m+1)\theta} \end{bmatrix} |K\rangle, \quad (10b)$$

$$|K'\rangle = \begin{bmatrix} 1 \\ 0 \end{bmatrix}, \quad |K\rangle = \begin{bmatrix} 0 \\ 1 \end{bmatrix}, \quad (10c)$$

here $|K\rangle$ and $|K'\rangle$ are valley spinors, $H_m^{(1)}$ and $H_m^{(2)}$ are Hankel functions of the first and second kind respectively, and $s = \text{sgn}(E)$. Now we can write the wavefunctions in terms of the scattering matrix S_m such that $\psi_m = \psi_m^{(\text{in})} + S_m \psi_m^{(\text{out})}$,

$$\Psi_m^{(\text{outer})}(r, \theta) = \sum_\alpha c_\alpha \psi_{m, \alpha}^{(\text{in})}(r, \theta) |\alpha\rangle + \sum_{\alpha, \beta} c_\alpha S_{m, \alpha \beta} \psi_{m, \beta}^{(\text{out})}(r, \theta) |\beta\rangle, \quad (11)$$

where $\alpha = K, K'$ and $\beta = K, K'$ are valley indexes. The symbol $S_{m, \alpha \beta}$ denotes the scattering from α to β valley, c_K and $c_{K'}$ are the weights of the valley polarization. We can obtain the coefficients for S_m , T_m^+ and T_m^- by applying the boundary conditions at $\Psi_m^{(\text{inner})}(R, \theta) = \Psi_m^{(\text{outer})}(R, \theta)$, as shown in Appendix A. Additionally, an incident plane-wave in the x -direction can be expressed with the aid of the Jacobi-Anger expansion as,

$$e^{ikr \cos \theta} = \sum_{m=-\infty}^{\infty} i^m J_m(kr) e^{im\theta}, \quad (12)$$

or equivalently as,

$$\Phi_0(r, \theta) = \sum_{m=-\infty}^{\infty} \sum_\alpha c_\alpha \frac{i^m}{2} [\psi_{m, \alpha}^{(\text{out})}(r, \theta) + \psi_{m, \alpha}^{(\text{in})}(r, \theta)] |\alpha\rangle. \quad (13)$$

The latter allows one to express $\Psi^{(\text{outer})}(r, \theta)$ in terms of the incoming plane and the outgoing waves, *i.e.*

$$\begin{aligned} \Psi^{(\text{outer})}(r, \theta) &= \Phi_0(r, \theta) \\ &+ \sum_{m=-\infty}^{\infty} \sum_{\substack{\alpha=K, K' \\ \bar{\alpha} \neq \alpha}} c_{\alpha} \frac{i^m}{2} \left[(S_{m, \alpha \alpha} - 1) \psi_{m, \alpha}^{(\text{out})}(r, \theta) |\alpha\rangle \right. \\ &\left. + S_{m, \alpha \bar{\alpha}} \psi_{m, \bar{\alpha}}^{(\text{out})}(r, \theta) |\bar{\alpha}\rangle \right], \end{aligned} \quad (14)$$

and the total wave function is obtained by,

$$\Psi(r, \theta) = \sum_{m=-\infty}^{\infty} \left[\Psi_m^{(\text{inner})}(r, \theta) + \Psi_m^{(\text{outer})}(r, \theta) \right]. \quad (15)$$

IV. VALLEY BIREFRINGENCE

Partially subjecting a graphene sheet to a gate potential that reverses its carriers character from electrons to holes between gated and non-gated regions leads to many interesting analogies between its electron dynamics and optical phenomena^{4,12,16}. The key ingredient to this phenomena is the reversal of the group velocity of quasiparticles between the regions with and without gate potentials. For example and to visualize the phenomena, we consider that the Fermi level of the system is $E_F > 0$, such that for the outer region it crosses the upper band. On the hand, in the inner region $E_F - V_0 < 0$ with $V_0 > 0$, which means that the Fermi level crosses the lower band. In this case (Fig. 1, with $\Delta_0 = 0$), for $r > R$ the quasiparticle's group velocity is parallel to the wavevector, *i.e.*, $v_g^{(\text{outer})} = v_f(k_{x,r(\text{outer})}\hat{x} + k_{y,r(\text{outer})}\hat{y})/|k_{r(\text{outer})}|$. In the inner region is anti-parallel $v_g^{(\text{inner})} = -v_f(k_{x,r(\text{inner})}\hat{x} + k_{y,r(\text{inner})}\hat{y})/|k_{r(\text{inner})}|$, here $k_{r(\text{inner})}$ ($k_{r(\text{outer})}$) is the wavevector in the inner (outer) region. Since, the group velocity is $v_g = dE(k)/d(\hbar k)$, if k is kept fixed, the sign of $E(k)$ changes for the valence and conduction bands, making it parallel to the Fermi momentum for n-type carriers, but anti-parallel for p-type⁶⁵.

The reversal of the group velocity from the outer to the inner region indicates that the gated region will act, in the semiclassical limit, as a circular electronic lens with a negative index of refraction $n = -k_{r(\text{inner})}/k_{r(\text{outer})}$, where $k_{r(\text{inner})}$ is the wave number inside the gated patch and $k_{r(\text{outer})}$ outside, and n is deduced from the electronic Snell's law^{4,18}. As shown in Fig. 1, in the limit $kR \gg 1$, the negative index of refraction leads to constructive interference between the different partial wave components and results in a probability density that forms cardioid caustics and cusps¹², in what mimics the optical caustics which arise from light refraction through a shaped medium and belong to a class of cusps in catastrophe theory¹³. Using differential geometry¹², the positions of the cusps for each $p - 1$ internal reflections can be shown to be

$$x_{cusp}(p) = \frac{(-1)^p}{|n| - 1 + 2p} R, \quad (16)$$

and in the case shown in Fig. 2 a), as the amplitude decreases with each internal reflection, we can clearly distinguish the cusps corresponding to $p = 1, 2$.

If in addition to the gate potential the circular region contains the Kekulé bond texture, then the electronic bands in this region will be characterized by $E_{\pm} = \pm \hbar v_f(1 \pm \Delta)|\mathbf{k}| + V_0$. Therefore, the gating of this region leads to the Fermi level intersecting the two degenerate bands, which are characterized by the two group velocities, $v_{g,\pm} = -v_f(1 \pm \Delta)$. Then, when $\Delta \neq 0$, in addition to the sign reversal of the group velocity between both regions we also have the two different group velocities in the inner region. Hence, the Kekulé patterned and gated region will act as a circular lens with two negative indices of refraction

$$n_{\pm} = -\frac{k_{\pm,r(\text{inner})}}{k_{r(\text{outer})}}, \quad (17)$$

with $k_{\pm,r(\text{inner})} = k_+$, k_- and are given in Eq. (8). As shown in Fig. 2b) The Kekulé patterning of the circular region results into the doubling of the cusps and caustics of the circular lens, which reflects its birefringent nature. The degree of birefringence can be characterized by $\zeta = |n_+ - n_-|$, and for the set of parameters in Fig. 2b) we get $\zeta \approx 0.25$. Moreover, the cusps locations is now modified to

$$x_{cusp}^{\pm}(p) = \frac{(-1)^p}{|n_{\pm}| - 1 + 2p} R, \quad (18)$$

and the spatial separation between the two cusps is found by $|x_{cusp}^+ - x_{cusp}^-|$. In Fig. 2 c) we show the valley preserving amplitude component, $|\psi_{K'K'}(r)|^2$, which retains the same valley component as the incoming electrons, and Fig. 2 d) the valley mixing component, $|\psi_{K'K}(r)|^2$, which flips the valley degree of freedom. From these figures we can notice that the Kekulé bond texture leads to the oscillation of the valley component as electrons travel in the patterned region, in what mimics the electron's spin-momentum coupling in the presence of a Rashba interaction^{14,16}.

V. LOW ENERGY SCATTERING

The scattering process can be further analyzed by obtaining the different types of cross sections, such as the total cross section σ_t which tells us the magnitude of the interaction between the incoming flux and the scattering region, the transport cross section σ_{tr} that describes the average momentum transfer during the scattering, and the skew cross section σ_{sk} which shows the asymmetry in the scattering around the axis of the incoming flux. This quantities can be obtained through the scattering amplitude $f(\theta)$, which can be found in the far field limit, *i.e.*,

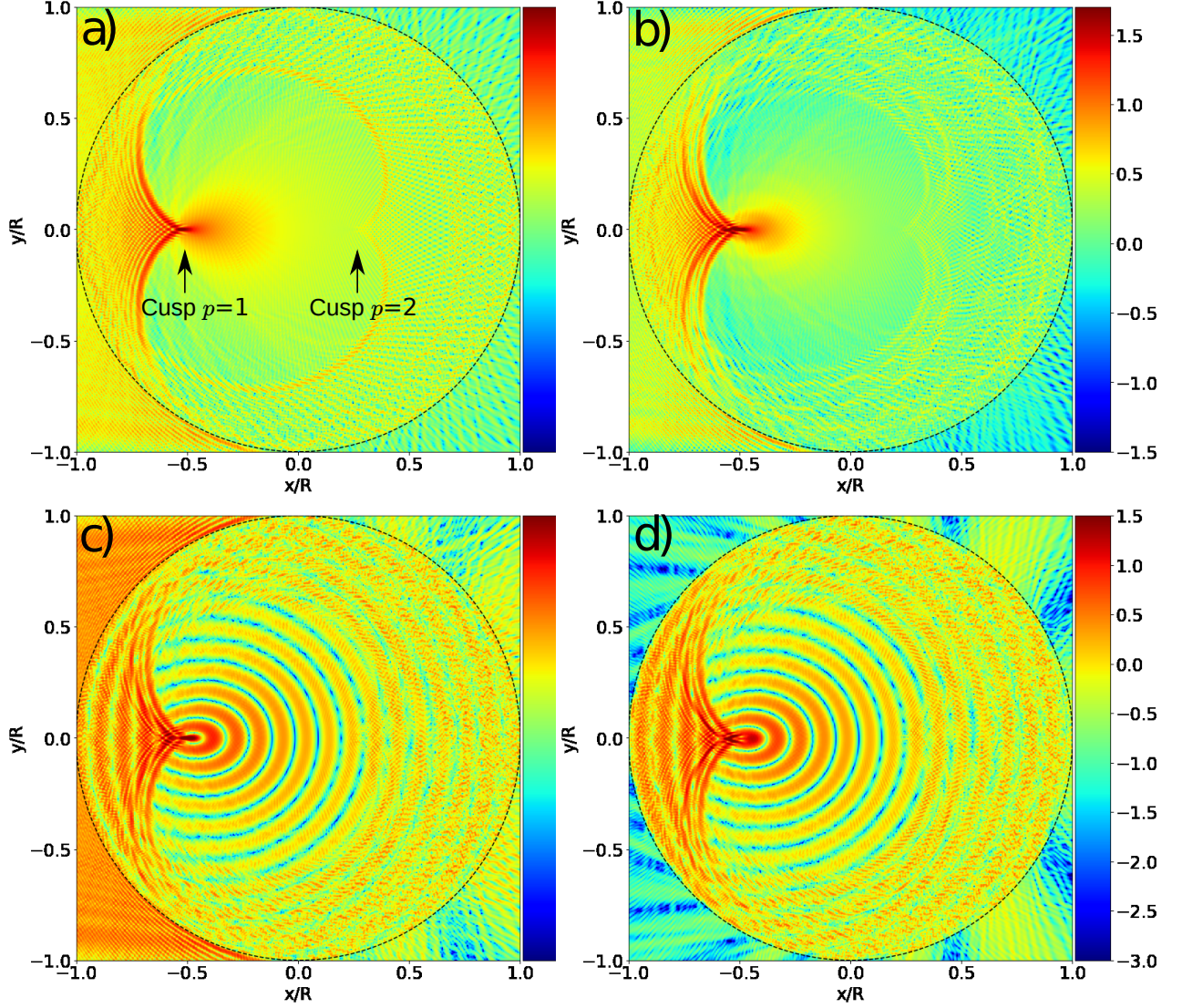


FIG. 2. Space dependence of the probability density (in \log_{10} scale), for an incoming electron flux in the x -direction with valley polarization K' and $kR = 300$. The dashed line shows the boundary between the scattering regions. A gate potential $V_0 R / (\hbar v_f) = 600$ is present in the inner region. For a) pristine graphene, b) Kekulé-Y distorted graphene in the $r < R$ region with $\Delta = 0.1$. The negative refractive index in addition to the circular geometry, leads to an interference pattern that forms a cardioid shaped envelope with a high concentration at the cusps, which split in two as we turn on the Kekulé distortion. The position of the cups is given by Eqs. (16) and (18) for the case of a) and b) respectively. Panel c) shows the valley-preserving component and d) the valley-flip component, for the case described in b). As the incoming electron enters the circular region their valley state begins to oscillate between K and K' [panels (c) and (d)]. The wavelength of the oscillation depends on the amplitude of Δ as this parameter characterizes the wavenumbers k_+ and k_- .

via the asymptotic form of the wave function as $r \rightarrow \infty$

$$\Psi(r \rightarrow \infty) \rightarrow \Phi_0 + \sum_m \sum_{\alpha, \beta} c_{\alpha} f_{m, \alpha \beta}(\theta) \frac{e^{ikr}}{\sqrt{r}} |\beta\rangle, \quad (19)$$

and using the asymptotic expansion of the Hankel functions,

$$H_m(kr)^{(1)/(2)} \rightarrow \sqrt{\frac{2}{\pi kr}} e^{\pm i(kr - \frac{m\pi}{2} - \frac{\pi}{4})}, \quad (20)$$

by comparing Eq. (14) to Eq. (19) we can deduce the scattering amplitude for each partial wave component in terms of the S matrix components

$$f_m = \frac{e^{-i\pi/4}}{\sqrt{2\pi k}} \begin{bmatrix} S_{m, K', K'} - 1 & -iS_{m, K', K} \\ iS_{m, K, K'} & S_{m, K, K} - 1 \end{bmatrix}, \quad (21)$$

where $S_{m, \alpha \beta}$ are the valley preserving ($\alpha = \beta$) and valley mixing scattering ($\alpha \neq \beta$) matrix elements corresponding to the m^{th} partial wave component (α and β represent the Dirac points, either K or K'). Then, for each pro-

cess (valley preserving and valley mixing), we find the corresponding differential cross section,

$$\sigma_{\alpha\beta}(\theta) = \left| \sum_{m=-\infty}^{\infty} f_{m,\alpha\beta} e^{im\theta} \right|^2, \quad (22)$$

total cross section,

$$\sigma_{t,\alpha\beta} = \int_{-\pi}^{\pi} \sigma_{\alpha\beta}(\theta) d\theta = 2\pi \sum_{m=-\infty}^{\infty} |f_{m,\alpha\beta}|^2, \quad (23)$$

transport cross section,

$$\begin{aligned} \sigma_{tr,\alpha\beta} &= \int_{-\pi}^{\pi} \sigma_{\alpha\beta}(\theta) (1 - \cos\theta) d\theta \\ &= \sigma_{t,\alpha\beta} - 2\pi \sum_{m=-\infty}^{\infty} \text{Re}(f_{m,\alpha\beta} f_{m+1,\alpha\beta}^*), \end{aligned} \quad (24)$$

and the skew cross section,

$$\begin{aligned} \sigma_{sk,\alpha\beta} &= \int_{-\pi}^{\pi} \sigma_{\alpha\beta}(\theta) \sin\theta d\theta \\ &= 2\pi \sum_{m=-\infty}^{\infty} \text{Im}(f_{m,\alpha\beta} f_{m+1,\alpha\beta}^*), \end{aligned} \quad (25)$$

by summing over all different allowed processes

$$\sigma_{\eta} = \sum_{\alpha,\beta} \sigma_{\eta,\alpha\beta}, \quad (26)$$

we obtain the total, transport, and skew cross sections ($\eta \in \{t, tr, sk\}$).

For low carrier concentrations and small regions with Kekulé bond texture ($kR \ll 1$) the most significant scattering channels are those of angular momentum $m = -1, 0, 1$. Within this regime, we show in Fig. 3 the total cross section against the strength of gate potential V_0 . In the absence of Kekulé patterning, the total cross section of the gated region displays one peak which uniquely arises from the valley preserving process and indicates the formation of quasi-bound states in this region with finite life-time characterized by the width of the peak^{17,66}. An increasing strength of the Kekulé interaction leads to the central (valley-preserving) peak height shrinking and its location shifting, while two new resonant (valley-mixing) peaks emerge. These two new peaks correspond to quasi-bound states forming due to valley mixing processes as it is shown in the inset of Fig. 3, and consequently their height increases with increasing values of Δ , as shown in Fig. 3.

When local interactions in a graphene sheet lead to the breaking of effective time reversal (time reversal per valley) while preserving the total time reversal, as is the case for the Kekulé patterning, it is possible to have a skew scattering, and by symmetry considerations it can be shown that¹⁷

$$\sigma_{sk,\alpha\alpha} = -\sigma_{sk,\bar{\alpha}\bar{\alpha}}, \quad (27a)$$

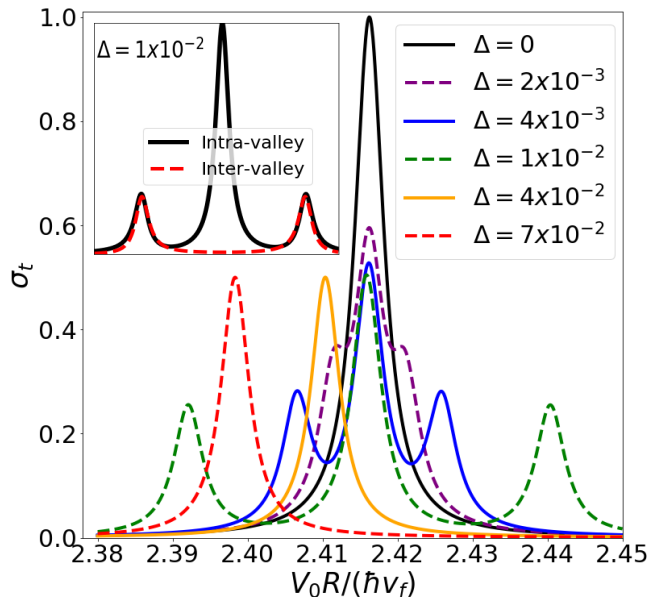


FIG. 3. Total cross section σ_t as a function of V_0 for incoming electrons in the x -direction with $kR = 1.5 \times 10^{-3}$. In the regime $kR \ll 1$ the resonances appear near the zeros of J_0 , here we show the resonances around the first one $\kappa_0^1 = 2.4048$ [see Appendix A, Eq. (A2a)]. (Inset) Total cross section for intra-valley $\sigma_{t,KK} + \sigma_{t,K'K'}$ and inter-valley $\sigma_{t,KK'} + \sigma_{t,K'K}$ process with $\Delta = 0.01$. To present the evolution of the inter-valley peaks, this figure only contains a zoom around the $\Delta = 0$ peak. Notice that the valley-mixing peaks are not shown in the figure for the largest two Δ values. These peaks are out of the figure range since Δ shifts the inter-valley peak and increases its separation from the intra-valley peaks.

$$\sigma_{sk,\alpha\bar{\alpha}} = 0. \quad (27b)$$

The latter equations indicate that electrons with opposite valley polarization get deflected towards opposite directions as they get scattered, thus producing a valley-Hall effect. To measure the asymmetry of the scattering per valley we calculate the skew parameter γ_V , which is defined as,

$$\gamma_V = \frac{1}{2}(\gamma_K - \gamma_{K'}), \quad (28a)$$

where the skew parameter for a valley $\beta = K$ or $\beta = K'$ is

$$\gamma_{\beta} = \frac{\sum_{\alpha} \sigma_{sk,\alpha\beta}}{\sum_{\alpha} \sigma_{tr,\alpha\beta}}, \quad (28b)$$

this quantity is directly connected to the transverse valley currents and is equal to the valley Hall angle at zero temperature in the absence of side-jump effects⁶⁷,

$$\Theta_{VH} = \frac{j_{VH}}{j_x} = \gamma_V. \quad (29)$$

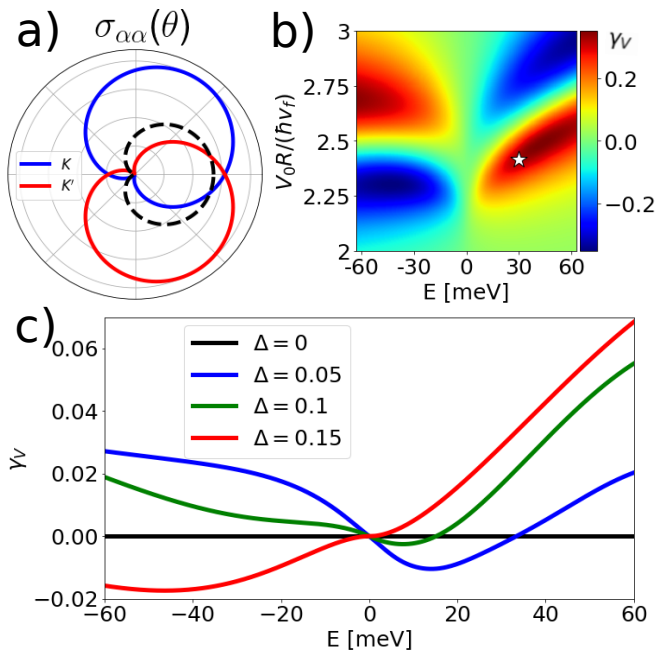


FIG. 4. a) Differential cross section for valley preserving processes, K -valley (blue) and K' -valley (red), showing the tilt of electrons with opposite valley-polarization towards opposite directions around the x -axis. The dashed black line in a) corresponds to the differential cross section without Kekulé distortion. b) Valley skew parameter γ_V as function of both energy and the gate potential for a region of $R = 9\text{\AA}$ and Kekulé amplitude $\Delta = 0.1$, the star marker indicates the values used for a). c) Average of γ_V as a function of energy for 4000 randomly sized Kekulé-Y regions ($9 \leq R \leq 18$ \AA), considering $V = 1$ eV and different values of Δ .

In the presence of the Kekulé-Y modulation, the valley asymmetry of scattering around the x -axis can be also deduced from the valley dependent differential cross section. In Fig 4 a), we present the differential cross section per valley for the set of parameters indicated by a star marker in Fig. 4 b). In contrast, we notice a symmetric scattering in the absence of the Kekulé-Y modulation, which is shown by the dashed black line in Fig 4 a). To show the dependence of the skew scattering in our system on the local potential of the Kekulé-Y patterned patches V_0 , and the Fermi energy (E), in Fig. 4 b) we show a map of the skew parameter, γ_V , as a function of V_0 and E for Kekulé patterned regions with $R = 9$ \AA and $\Delta = 0.1$. In the latter we should note that the regions of high γ_V coincide with the regions of resonant scattering, *i.e.*, resonant regime in the total cross section (Fig. 3), and which indicates that skew scattering is resonantly enhanced⁶⁷. To demonstrate the robustness of skew scattering in the system to variations in size of the Kekulé-Y patterned patches, we consider a uniform random distribution of impurity sizes in the dilute limit. In Fig. 4 c) we show the average of γ_V for different values of Δ and V_0 . Since skew scattering is resonantly enhanced, then its detection

survives the random variations in the sizes of the Kekulé patterned patches in the dilute limit, and which allows for the detection of valley Hall effect signatures in transport experiments. We also note that since the $RV_0/(\hbar v_f)$ governs the appearance of the different scattering regimes in Fig. 3, then skew scattering is also robust to variations in the locally enhanced potential.

Let us briefly discuss a suitable set of parameters. Δ is fixed by the Kekulé pattern bond modulation, which we will suppose as others³⁷ of order $\Delta \approx 0.1$ although, in principle, its value can be varied by applying strain^{41,68}, a way to determine this parameter is by modeling the Kekulé lattice using a DFT approach and obtaining an effective tight-binding model. The experimental setup can vary the two parameters V_0 and R . For example, in Fig. 4 we presented the results for patches of size $R = 9$ \AA, which is the minimal size to have multiple unit cells in the patch regions, so we can still apply our low energy continuum model, values above that will be also valid. From the figure, we see that detection will involve the condition $V_0 R / \hbar v_f \approx 2.42$ from where we obtain a gate voltage of around 0.66 eV. From there, V_0 can be diminished at will.

VI. CONCLUSIONS

We have studied the scattering of Dirac Fermions from Kekulé distorted and gated regions in graphene. For large Kekulé patterned and gated regions, we have shown that the scattering of electrons from these circular patches leads to the formation of caustics and cusps reminiscent of a circular birefringent electronic lens with two negative indices of refraction. Moreover, the separation of the cusps in the circular lens is proportional to the Kekulé interaction and provides a direct measure of its strength in systems with tailored Kekulé patches.

For low carrier concentrations, we have shown that the presence of scatterers with a locally enhanced Kekulé interaction and gate potential leads to the electrons from different valleys deflecting in opposite directions due to the skew scattering produced by the Kekulé distortion. Skew scattering in the system leads to the appearance of a valley Hall effect. We have also shown that the skew scattering-generated valley Hall effect can be present in systems where the Kekulé patterning is not uniform but when it consists of patches with random sizes and potentials. The latter suggests the plausible experimental realization and detection of the skew scattering induced valley Hall effect in Kekulé patterned graphing systems via four probe experiments. Also, it may be worth extending this study to other short-wavelength modulations, for example, for $\sqrt{3} \times \sqrt{3}$ superlattices and twisted multilayered graphene⁶⁹.

Therefore, valley birefringence directly measures the presence of Kekulé-Y distortion, and its strength relates to wavefronts separation at the cusps. In the case of low-carrier concentrations, the combination of Kekulé distur-

tion and gate potential can lead to an asymmetric scattering between valleys and thus produce a valley-Hall effect, even if the Kekulé pattern is not uniform.

Optical birefringence allows the identification of internal anisotropies, stresses, and space inhomogeneities of materials and even allows decoupling polarized modes in optical fibers. Consequently, our results could serve to design configurations that discern broken symmetries and thus be used to design valley decoupled electronic analogs to optical fibers.

VII. ACKNOWLEDGMENTS

E.A. and R.C.B. acknowledges useful discussions with Alex Santacruz. This work was supported by UNAM DGAPA PAPIIT IN102620 (E.A. and G.G.N.), CONA-CyT project 1564464 (E.A. and G.G.N.), and the National Science Foundation via Grant No. DMR-2213429 (M.M.A.).

Appendix A: Boundary Conditions

In this appendix we find explicit solutions for the coefficients in Sec. III, which are found by solving for the boundary conditions. The solution of the system of equations resulting from the boundary condition $\Psi_m^{(\text{inner})}(R, \theta) = \Psi_m^{(\text{outer})}(R, \theta)$ gives us the following analytical expressions for the S_m matrix elements and the amplitudes T_m^\pm ,

$$S_{m,K'K'} = ss'(H_m^{(1)}H_{m-1}^{(2)}X_m + H_{m+1}^{(1)}H_m^{(2)}X_{m-1})/D_m - (2H_{m+1}^{(1)}H_{m-1}^{(2)}Q_m + H_m^{(1)}H_m^{(2)}Z_m)/D_m, \quad (\text{A1a})$$

$$S_{m,KK} = ss'(H_{m-1}^{(1)}H_m^{(2)}X_m + H_{m+1}^{(1)}H_{m+1}^{(2)}X_{m-1})/D_m - (2H_{m-1}^{(1)}H_{m+1}^{(2)}Q_m + H_m^{(1)}H_m^{(2)}Z_m)/D_m, \quad (\text{A1b})$$

$$S_{m,K'K} = \frac{-ss'Y_m P_m}{D_m}, \quad (\text{A1c})$$

$$S_{m,KK'} = \frac{-ss'Y_{m-1} P_{m+1}}{D_m}, \quad (\text{A1d})$$

$$T_m^+ = c_1(j_{m+1}^- H_m^{(1)} - ss'j_m^- H_{m+1}^{(1)})P_m/D_m + c_2(j_{m-1}^- H_m^{(1)} - ss'j_m^- H_{m-1}^{(1)})P_{m+1}/D_m, \quad (\text{A1e})$$

$$T_m^- = c_1(j_{m+1}^+ H_m^{(1)} - ss'j_m^+ H_{m+1}^{(1)})P_m/D_m - c_2(j_{m-1}^+ H_m^{(1)} - ss'j_m^+ H_{m-1}^{(1)})P_{m+1}/D_m, \quad (\text{A1f})$$

where we defined,

$$D_m = -ss'(H_m^{(1)}H_{m-1}^{(1)}X_m + H_{m+1}^{(1)}H_m^{(1)}X_{m-1}) + 2H_{m+1}^{(1)}H_{m-1}^{(1)}Q_m + H_m^{(1)}H_m^{(1)}Z_m, \quad (\text{A2a})$$

$$X_m = j_m^+ j_{m+1}^- + j_{m+1}^+ j_m^-, \quad (\text{A2b})$$

$$Y_m = j_m^+ j_{m+1}^- - j_{m+1}^+ j_m^-, \quad (\text{A2c})$$

$$Z_m = j_{m-1}^+ j_{m+1}^- + j_{m+1}^+ j_{m-1}^-, \quad (\text{A2d})$$

$$Q_m = j_m^+ j_m^-, \quad (\text{A2e})$$

$$P_m = H_m^{(1)}H_{m-1}^{(2)} - H_{m-1}^{(1)}H_m^{(2)}, \quad (\text{A2f})$$

here all Hankel functions are evaluated at kR and $j_m^\pm = J_m(k_\pm R)$.

* eandrade@estudiantes.fisica.unam.mx

¹ D. Dragoman and M. Dragoman, *Quantum-classical analogies* (Springer Science & Business Media, 2004).

² M. Katsnelson, K. Novoselov, and A. Geim, *Nature physics* **2**, 620 (2006).

³ K. S. Novoselov, A. K. Geim, S. V. Morozov, D. Jiang, Y. Zhang, S. V. Dubonos, I. V. Grigorieva, and A. A. Firsov, *Science* **306**, 666 (2004).

⁴ V. V. Cheianov, V. Fal'ko, and B. Altshuler, *Science* **315**, 1252 (2007).

⁵ G.-H. Lee, G.-H. Park, and H.-J. Lee, *Nature Physics* **11**, 925 (2015).

⁶ S.-H. Zhang, W. Yang, and F. M. Peeters, *Phys. Rev. B* **97**, 205437 (2018).

⁷ S.-H. Zhang and W. Yang, *New Journal of Physics* **21**, 103052 (2019).

⁸ Y. Betancur-Ocampo, *Phys. Rev. B* **98**, 205421 (2018).

⁹ F. Libisch, T. Hirsch, R. Glattauer, L. A. Chizhova, and J. Burgdrfer, *Journal of Physics: Condensed Matter* **29**, 114002 (2017).

¹⁰ J. Williams, T. Low, M. Lundstrom, and C. Marcus, *Nature nanotechnology* **6**, 222 (2011).

¹¹ Y. Betancur-Ocampo, F. Leyvraz, and T. Stegmann, *Nano letters* **19**, 7760 (2019).

¹² J. Cserti, A. Pályi, and C. Péterfalvi, *Physical review letters* **99**, 246801 (2007).

¹³ M. Berry and C. Upstill (Elsevier, 1980), vol. 18 of *Progress in Optics*, pp. 257–346.

¹⁴ Y. A. Bychkov and E. I. Rashba, *JETP Lett.* **39**, 78 (1984).

- ¹⁵ C. L. Kane and E. J. Mele, Phys. Rev. Lett. **95**, 226801 (2005).
- ¹⁶ M. M. Asmar and S. E. Ulloa, Physical Review B **87**, 075420 (2013).
- ¹⁷ M. M. Asmar and S. E. Ulloa, Physical Review B **91**, 165407 (2015).
- ¹⁸ A. H. Castro Neto, F. Guinea, N. M. R. Peres, K. S. Novoselov, and A. K. Geim, Rev. Mod. Phys. **81**, 109 (2009).
- ¹⁹ M. I. Katsnelson and M. I. Katsnelson, *Graphene: carbon in two dimensions* (Cambridge university press, 2012).
- ²⁰ V. K. Joshi, Engineering Science and Technology, an International Journal **19**, 1503 (2016), ISSN 2215-0986.
- ²¹ I. Žutić, J. Fabian, and S. Das Sarma, Rev. Mod. Phys. **76**, 323 (2004).
- ²² A. Rycerz, J. Tworzydło, and C. W. J. Beenakker, Nature Phys. **3** (2007).
- ²³ D. Gunlycke and C. T. White, Phys. Rev. Lett. **106**, 136806 (2011).
- ²⁴ J.-H. Chen, G. Autès, N. Alem, F. Gargiulo, A. Gautam, M. Linck, C. Kisielowski, O. V. Yazyev, S. G. Louie, and A. Zettl, Phys. Rev. B **89**, 121407 (2014).
- ²⁵ Y. Liu, J. Song, Y. Li, Y. Liu, and Q.-F. Sun, Phys. Rev. B **87**, 195445 (2013).
- ²⁶ Z. Liu, L. Jiang, and Y. Zheng, J. Phys.: Cond. Matt. **27**, 045501 (2015).
- ²⁷ F. Zhai, X. Zhao, K. Chang, and H. Q. Xu, Phys. Rev. B **82**, 115442 (2010).
- ²⁸ M. Ramezani Masir, A. Matulis, and F. M. Peeters, Phys. Rev. B **84**, 245413 (2011).
- ²⁹ D. Moldovan, M. Ramezani Masir, L. Covaci, and F. M. Peeters, Phys. Rev. B **86**, 115431 (2012).
- ³⁰ J. Wang and S. Fischer, Phys. Rev. B **89**, 245421 (2014).
- ³¹ J. L. Garcia-Pomar, A. Cortijo, and M. Nieto-Vesperinas, Phys. Rev. Lett. **100**, 236801 (2008).
- ³² Y. Jiang, T. Low, K. Chang, M. I. Katsnelson, and F. Guinea, Phys. Rev. Lett. **110**, 046601 (2013).
- ³³ M. M. Grujić, M. Tadić, and F. M. Peeters, Phys. Rev. Lett. **113**, 046601 (2014).
- ³⁴ M. M. Asmar and S. E. Ulloa, Phys. Rev. B **96**, 201407 (2017).
- ³⁵ C.-Y. Hou, C. Chamon, and C. Mudry, Phys. Rev. Lett. **98**, 186809 (2007).
- ³⁶ C. Chamon, Phys. Rev. B **62**, 2806 (2000).
- ³⁷ O. Gamayun, V. Ostroukh, N. Gnezdilov, I. Adagideli, and C. Beenakker, New Journal of Physics **20**, 023016 (2018).
- ³⁸ C. Gutiérrez, C.-J. Kim, L. Brown, T. Schiros, D. Nordlund, E. B. Lochocki, K. M. Shen, J. Park, and A. N. Pasupathy, Nature Physics **12**, 950 (2016).
- ³⁹ C. Bao, H. Zhang, T. Zhang, X. Wu, L. Luo, S. Zhou, Q. Li, Y. Hou, W. Yao, L. Liu, et al., Phys. Rev. Lett. **126**, 206804 (2021).
- ⁴⁰ C. Bao, H. Zhang, X. Wu, S. Zhou, Q. Li, P. Yu, J. Li, W. Duan, and S. Zhou, Phys. Rev. B **105**, L161106 (2022).
- ⁴¹ D. Eom and J.-Y. Koo, Nanoscale **12**, 19604 (2020).
- ⁴² A. Qu, P. Nigge, S. Link, G. Levy, M. Michiardi, P. Spandaru, T. Matthé, M. Schneider, S. Zhdanovich, U. Starke, et al., Science Advances **8**, eabm5180 (2022).
- ⁴³ M.-H. Zhang, Y.-N. Ren, Q. Zheng, X.-F. Zhou, and L. He, *Stabilizing sample-wide Kekulé orders in graphene/transition metal dichalcogenide heterostructures* (2022), arXiv:2208.01286.
- ⁴⁴ Y. Mohammadi and S. Bahrami, Chinese Physics B **31**, 017305 (2022).
- ⁴⁵ E. Andrade, R. Carrillo-Bastos, P. A. Pantalen, and F. Mireles, Journal of Applied Physics **127**, 054304 (2020).
- ⁴⁶ S. A. Herrera and G. G. Naumis, Phys. Rev. B **101**, 205413 (2020).
- ⁴⁷ S. A. Herrera and G. G. Naumis, Phys. Rev. B **102**, 205429 (2020).
- ⁴⁸ Y. Mohammadi, ECS Journal of Solid State Science and Technology **10**, 061011 (2021).
- ⁴⁹ A. Santacruz, P. E. Iglesias, R. Carrillo-Bastos, and F. Mireles, Phys. Rev. B **105**, 205405 (2022).
- ⁵⁰ J. J. Wang, S. Liu, J. Wang, and J.-F. Liu, Phys. Rev. B **98**, 195436 (2018).
- ⁵¹ E. Andrade, R. Carrillo-Bastos, and G. G. Naumis, Phys. Rev. B **99**, 035411 (2019).
- ⁵² D. A. Ruiz-Tijerina, E. Andrade, R. Carrillo-Bastos, F. Mireles, and G. G. Naumis, Phys. Rev. B **100**, 075431 (2019).
- ⁵³ Q.-P. Wu, L.-L. Chang, Y.-Z. Li, Z.-F. Liu, and X.-B. Xiao, Nanoscale research letters **15**, 1 (2020).
- ⁵⁴ J. J. Wang, S. Liu, J. Wang, and J.-F. Liu, Phys. Rev. B **101**, 245428 (2020).
- ⁵⁵ W. Zeng and R. Shen, Phys. Rev. B **104**, 075436 (2021).
- ⁵⁶ S. G. y. García, T. Stegmann, and Y. Betancur-Ocampo, Phys. Rev. B **105**, 125139 (2022).
- ⁵⁷ E. Andrade, G. G. Naumis, and R. Carrillo-Bastos, Journal of Physics: Condensed Matter **33**, 225301 (2021).
- ⁵⁸ H. Ochoa, A. H. Castro Neto, V. I. Fal'ko, and F. Guinea, Phys. Rev. B **86**, 245411 (2012).
- ⁵⁹ C. Beenakker, Reviews of Modern Physics **80**, 1337 (2008).
- ⁶⁰ E. McCann and V. I. Falko, Journal of Physics: Condensed Matter **16**, 2371 (2004).
- ⁶¹ D. J. Alspaugh, M. M. Asmar, D. E. Sheehy, and I. Vekhter, Phys. Rev. B **105**, 054502 (2022).
- ⁶² E. Thareja, I. Vekhter, and M. M. Asmar, Phys. Rev. B **102**, 125308 (2020).
- ⁶³ M. Tanhayi Ahari, G. Ortiz, and B. Seradjeh, American Journal of Physics **84**, 858 (2016).
- ⁶⁴ L. Isaev, G. Ortiz, and I. Vekhter, Phys. Rev. B **92**, 205423 (2015).
- ⁶⁵ S. Chen, Z. Han, M. M. Elahi, K. M. Habib, L. Wang, B. Wen, Y. Gao, T. Taniguchi, K. Watanabe, J. Hone, et al., Science **353**, 1522 (2016).
- ⁶⁶ M. M. Asmar and S. E. Ulloa, Phys. Rev. Lett. **112**, 136602 (2014).
- ⁶⁷ A. Ferreira, T. G. Rappoport, M. A. Cazalilla, and A. C. Neto, Physical review letters **112**, 066601 (2014).
- ⁶⁸ D. Q. Khoa, C. V. Nguyen, L. M. Bui, H. V. Phuc, B. D. Hoi, N. V. Hieu, V. Q. Nha, N. Huynh, L. C. Nhan, and N. N. Hieu, Materials Research Express **6**, 045605 (2019).
- ⁶⁹ S. A. Herrera and G. G. Naumis, Phys. Rev. B **104**, 115424 (2021).